Supporting Information for

Matrix Effects Reshape Organic Aerosol Volatility and Atmospheric Persistence

Qiaorong Xie,[1] Abigail M. Smith,[1] Sara C. Botero-Carrizosa,[1] Steven A. L. Sharpe,[1] Gali Dekel,[3] Nicole A. June,[4] Manish Shrivastava,[4] Yuqing Dai,[5] Kevin Ridgway,[6] Christian L'Orange,[6] Shantanu H. Jathar,[6] Katherine S. Hopstock,[7] Sergey A. Nizkorodov,[7] Yinon Rudich,[3] Alexander Laskin[1,2]*

[1] Department of Chemistry, [2]Department of Earth, Atmospheric, and Planetary Sciences, Purdue University, West Lafayette, Indiana, 47907, United States

[3]Department of Earth and Planetary Sciences, Weizmann Institute of Science, Rehovot 76100, Israel

[4]Atmospheric, Climate, and Earth Sciences Division, Pacific Northwest National Laboratory, Richland, Washington, 99352, United States

[5]School of Geography, Earth and Environmental Science, University of Birmingham, Birmingham, B15 2TT, United Kingdom

[6]Department of Mechanical Engineering, Colorado State University, Fort Collins, Colorado 80523, United States

[7]Department of Chemistry, University of California, Irvine, Irvine, California 92697, United States

**Corresponding author: Alexander Laskin (alaskin@purdue.edu)*

TABLE OF CONTENTS

Supplemental Note 1. Details of TPD-DART-HRMS experiments and data analysis, molecular metric calculations.

TPD-DART-HRMS experimental details. A direct analysis in real time (DART, JumpShot®) ambient ionization source (IonSense Inc., Saugus, MA) equipped with VAPUR® API interface and a thermal desorption/pyrolysis stage (ionRocketTM, BioChromato Inc., Fujisawa, Kanagawa, Japan) was used to thermally desorb components of organic mixture samples over the time of the temperature programmed desorption (TPD).[1, 2, 3] Each of the filter-collected samples (mixtures S, A, W, F, P) were sectioned and mounted onto a copper stub nested within the TPD heating block, whereas condensate samples (mixture G, E, B) were pipetted (~6 μL) directly into the well at the center of the copper stub. The temperature ramping profile started at 298 K, held for 0.4 min, followed by a linear ramp at a rate of 70 K min^{-1} to 623 K, and then maintained at the final temperature for 2 min. The volatilized components were directed into the T-shaped glass junction, where they were ionized by metastable He atoms in the DART gas stream at a flow rate of 2 L min^{-1}. The DART ionization source dynamically ionized the gas-phase species degassing from the samples during the TPD experimental runs, which were subsequently detected by the interfaced Q-Exactive HF-X Orbitrap mass analyzer operated at mass resolution of $m/\Delta m$ ~ 240,000 at 200 m/z. The high-resolution mass spectrometer (HRMS) and DART ion source parameters were: 200 °C capillary temperature, 80 RF S-lens level, 100 ms integration time, 100°C DART heater temperature, and -3.5 V grid voltage applied to electrode inside DART skimmer cone. Progression of the high-resolution mass spectra was recorded to identify individual components.

TPD-DART-HRMS data analysis. The HRMS peak lists were inferred from total ion thermograms recorded in TPD experiments, integrated over elution times, and were background subtracted using the Xcalibur software.[1] Peak lists were extracted with the Decon2LS software developed at Pacific Northwest National Laboratory (PNNL) (http://omics.pnl.gov/software/)[4] and processed using Excel macros developed for *m/z* peak alignment, blank subtraction, and C^{13} isotope clustering and filtering[4]. Molecular formulas were assigned based on the high order mass defect analysis of the two-dimensional homologous series of HRMS peaks, which clusters peaks differing by the number of $-CH_2$, $-H_2$, and -O units into the same group. Molecular formulas were assigned based on the ions detected in negative mode, (–)DART-HRMS in the m/z range of 100–1000 Da, with constraints of $C_{1\text{-}40}H_{1\text{-}100}O_{1\text{-}25}N_{0\text{-}1}$ and mass tolerance of ±2.0 ppm.[5] In these

experiments, the (–)DART ionization mechanism led to the formation of deprotonated molecules $[M-H]^-$ and radical anions $M^{-\bullet}$.

Consequently, the apparent saturation vapor pressure ${}^{i}p_T^*$ (Pa) of each component (*i*) as a function of temperature (*T*) are determined using the simplified Clausius-Clapeyron equation (Eq. S1),[6] which assumes that volatility is primarily governed by the enthalpy term (${}^{i}\Delta H^*$), while entropy contributions (${}^{i}\Delta S^*$) are relatively small and comparable across components. The values of saturation vapor pressure are then converted to saturated mass concentrations ${}^{i}C_T^*$ (μg m^{-3}) based on the ideal gas equation (Eq. S2). These calculations require input values of ${}^{i}T_{max}^*$, ${}^{i}\Delta H^*$, ${}^{i}p_{T_{max}}^*$, and molecular weight of $C_xH_yO_z$ species *i* (${}^{i}MW$), all inferred from the TPD-DART-HRMS records.[1, 3] ${}^{i}T_{max}^*$corresponds to the peak ion intensity in the extracted ion thermograms of individual species. The values of ${}^{i}\Delta H^*$ are derived from the slope of Arrhenius plots. The reference vapor pressure ${}^{i}P_{T_{max}}^*$of the individual species (*i*) is estimated by assuming the stoichiometry of its formal combustion oxidation reaction, as described in our earlier publication.[1] *R* denotes the molar gas constant with value of 8.3145 J mol^{-1} K^{-1}.

$$ {}^{i}p_T^* = {}^{i}p_{T_{max}}^* \times exp\left[\left(-\frac{{}^{i}\Delta H^*}{R}\right)\left(\frac{1}{T}-\frac{1}{T_{max}^*}\right)\right] \quad \text{(S1)} $$

$$ {}^{i}C_T^* = \frac{{}^{i}p_T^* \times 10^9 \times {}^{i}MW}{RT} \quad \text{(S2)} $$

Although structural isomers sharing the same elemental formula can exhibit different volatility parameters due to differences in molecular structure and physicochemical properties, no structural information beyond elemental composition is available in the present dataset. Consequently, features assigned to the same elemental formula may include contributions from multiple unresolved isomers, and the reported volatility parameters should be interpreted as elemental-formula-resolved properties rather than properties of uniquely identified molecular species.

During the TPD ramp, the aerosol matrix is not compositionally static. As more volatile constituents are preferentially removed, the residual condensed phase becomes progressively enriched in lower-volatility material. This evolving matrix can alter activity coefficients, phase state, viscosity, and internal mass-transfer limitations, thereby influencing the shapes and peak positions of extracted ion thermograms. Consequently, the fitted ${}^{i}\Delta H^*$ and $\log({}^{i}C_{298K}^*)$ values should be interpreted as experimentally derived,

component-resolved apparent volatility parameters rather than equilibrium properties of pure compounds at fixed composition. This behavior is also relevant to atmospheric OA, where changing environmental conditions continuously drive gas-particle partitioning and alter particle-phase composition and physical state. Although the TPD ramp spans a broader temperature range and occurs on a shorter timescale than typical atmospheric variability, volatility in both systems is governed by an evolving multicomponent matrix. Thus, the apparent volatility parameters derived here are consistent with the matrix-dependent volatility effects that influence the behavior of OA under real atmospheric conditions. All measurements reported here were performed under dry conditions. In atmospheric OA, water can influence volatility through several coupled mechanisms, including dilution of the organic matrix, modification of activity coefficients, disruption of organic-organic hydrogen-bonding networks, plasticization of the condensed phase, and reduced viscosity (enhanced molecular diffusion). Accordingly, the volatility parameters reported here should be interpreted as dry-matrix apparent volatilities, whereas additional measurements under humidified conditions or in aqueous systems will be needed to elucidate the role of water in matrix-controlled volatility.

Molecular metric calculations. Characteristic molecular metrics (*mm*) were calculated for the identified neutral molecular species (*i*), including molecular weight (*MW*), carbon oxidation state (OS_C), elemental ratios (*H/C, O/C, N/C*), modified aromaticity index (*AI*), double bond equivalent (*DBE*), and component-specific glass transition temperature (T_g). The equations used to calculate OS_C, *AI*, and *DBE* (Eqs. S3–S5) are listed below.[7]

$$OS_C = 2\frac{O}{C} - \frac{H}{C} - 3\frac{N}{C} \quad \text{(S3)}$$

$$AI = \frac{1+C-0.5O-S-0.5H}{C-0.5O-S-N} \quad \text{(S4)}$$

$$DBE = 1 + C - \frac{H}{2} + \frac{N}{2} \quad \text{(S5)}$$

where *C, H, O, N, and S* are the corresponding number of carbon, hydrogen, oxygen, nitrogen, and sulfur atoms.

The component-specific glass transition temperature (T_g) is estimated using a parameterization method based on the number of carbon (n_C), hydrogen (n_H), and oxygen (n_O) atoms in the corresponding elemental formula. For CH and CHO compounds, the estimation employs Equation S6 along with parameter values for n_C^0, b_C, b_H, b_{CH}, b_O, and b_{CO} of 1.96, 61.99, −113.33,

28.74, 0, and 0 for CH compounds and 12.13, 10.95, −41.82, 21.61, 118.96, and −24.38 for CHO compounds.[8]

$$T_{g,i} = (n_C^o + \ln(n_C))b_C + \ln(n_H)\, b_H + \ln(n_C)\ln(n_H)\, b_{CH} + \ln(n_O)\, b_O + \ln(n_C)\ln(n_O)\, b_{CO} \quad \text{(S6)},$$

For CHON compounds, the estimation employs Equation S7 along with parameter values for coefficients for n_C^0, b_C, b_O, b_N, b_{CO}, b_{CN}, and b_{ON} of 5.34, 31.53, −7.06, 134.96, 6.54, −34.36, and −15.35, respectively.[9]

$$T_{g,i} = (n_C^o + \ln(n_C))b_C + \ln(n_N)\, b_N + \ln(n_C)\ln(n_N)\, b_{CN} + \ln(n_O)\, b_O + \ln(n_C)\ln(n_O)\, b_{CO} + \ln(n_N)\ln(n_O)\, b_{ON} \quad \text{(S7)},$$

Mole fractions (x_i) of the individual species were approximated as follows (Eq. S8):

$$x_i = {}^{h_i}/_{h_{total}} \quad \text{(S8)},$$

where h_i is the integrated area of the single ion thermogram for species i and h_{total} is the integrated area of the total negative ion thermogram, assuming proportionality between ion signal and concentration. Note that Arrhenius plots could be constructed only for a subset of sufficiently abundant species. Consequently, the calculated (x_i) values do not sum to unity for a given sample because additional low-intensity species, which contribute to h_{total} but their volatility cannot be quantified.

To assess the relative influence of compound-specific versus mixture-dependent properties, we use the products of $mm_i \times x_i$ to describe individual species and their mixture-averaged values $<mm_i \times x_i>$ to represent each analyzed mixture as a whole, determined by Eq. (S9):

$$< mm_i \times x_i > = \sum mm_i \times x_i \quad \text{(S9)},$$

where *mm* corresponds to any of the molecular metrics listed above. Complete list of the individual species, their ${}^i\Delta H^*$, $\log({}^iC^*_{298K})$, $mm_i \times x_i$, and $<mm_i \times x_i>$ values reported in this study is provided in a Supplemental File 'TPD-DART-HRMS data summary with species metrics.xlsx'.

Table S1. Organic aerosol mixtures examined in this study, including sample identifiers and brief descriptions of their sources, production, or collection procedures. The complete list of assigned individual species, their corresponding ${}^{i}\Delta H^{*}$, $\log({}^{i}C^{*}_{298K})$, x_i, and other descriptors, is provided in the supplementary data file 'Dataset S1.xlsx'.

Sample Type	ID	Additional Description	Refs.	Lines (#) in the supplementary data file.
Laboratory generated Secondary Organic Aerosol (SOA) from ozonolysis of monoterpenes	S1	Samples of laboratory α-pinene-SOA (S1), limonene-SOA (S2) and ocimene-SOA (S3) generated in an environmental chamber at Purdue University.	1, 3, 10, 11	1-59
	S2			60-116
	S3			117-147
Mixtures of reference organic compounds common in biomass burning emissions	G1	Authentic BrC standard samples were prepared as 100 ppm stock solutions in methanol and organized into four groups (G1–G4), each consisting of 25 distinct species. Courtesy of the University of North Carolina, group of Prof J. Surratt.	12, 13 Volatility data is reported in this work	148-164
	G2			165-173
	G3			174-184
	G4			185-195
Laboratory generated proxies of biomass burning organic aerosol (BBOA)	B1	Samples generated from the pyrolysis of hardwood pellets in lab at Weizmann Institute of Science, Rehovot, Israel, produced an initial PO_1 condensate (B1). PO_1 was subsequently evaporated down to 75% of its initial volume, producing a second $PO_{1.33}$ condensate (B2).	14, 15, 16, 17	196-248
	B2			249-303
Field collected anthropogenic organic aerosols (OA)	A1	Ambient OA samples were collected at 15m (A1) and 200m (A2) altitudes using an UAV-mounted Portable Aethalometer during the Lag Ba'Omer festival at the campus of the Weizmann Institute of Science, Rehovot, Israel.	18	304-345
	A2			346-384
Laboratory generated mixtures of organic aerosol (OA) from pyrolysis of construction materials	W1a	OA samples generated in a pyrolysis chamber at University of California, Irvine, CA, from commercial construction materials including douglas fir (W1a, W1b, W1c), medium-density fiberboard (F1a, F1b, F1c), fiberboard (F2), phenol urea formaldehyde (P1), carpet (P2), and vinyl tile (P3).	13, 19 Volatility data is reported in this work	385-468
	W1b			469-546
	W1c			547-631
	F1a			632-700
	F1b			701-774
	F1c			775-857
	F2			858-873
	P1			874-944
	P2			945-958
	P3			960-987
Test facility generated mixtures of organic aerosol (OA) from pyrolysis of construction materials	W11	OA samples generated in a test facility chamber at Colorado State University, Fort Collins, CO, from pyrolysis of commercial construction materials including douglas fir (W11), southern yellow pine (W12), structural wood mix (W13), medium-density fibreboard (F11), plywood (F12), oriented strand board (F13), extruded polystyrene (P11), and phenol urea formaldehyde (P12).	20 Volatility data is reported in this work	988-1051
	W12			1052-1137
	W13			1138-1202
	F11			1203-1268
	F12			1269-1322
	F13			1323-1386
	P11			1387-1449
	P12			1450-1477
E-cigarette mixtures	E1	Commercial E-cigarette liquids.	Volatility data is reported in this work	1478-1513
	E2			1514-1531
	E3			1532-1540
	E4			1541-1549

Supplemental Note 2. Thermodynamic coupling between ${}^{i}\Delta H^{*}$ and $\log {}^{i}C^{*}_{298K}$ values of individual species.

The integrated Clausius–Clapeyron equation, including both enthalpy and entropy terms, written for an effective saturation vapor pressure (${}^{i}p^{*}_{T}$, Pa) of species (*i*):

$$2.303 \times log\ {}^{i}p^{*}_{T} = -\frac{{}^{i}\Delta H^{*}}{RT} + \frac{{}^{i}\Delta S^{*}}{R} + Const \tag{S10}$$

where ${}^{i}\Delta H^{*}$ (kJ·mol^{-1}) is the apparent condensed-to-gas phase transition enthalpy; ${}^{i}\Delta S^{*}$ (J mol^{-1} K^{-1}) is the corresponding entropy term; R is the universal gas constant; *Const* is an integration constant; 2.303 is a conversion factor from *ln* to log_{10}.

Rearranging Eq. S10 for enthalpy, the expression is derived for ${}^{i}\Delta H^{*}$ versus ${}^{i}p^{*}_{T}$:

$${}^{i}\Delta H^{*} = -2.303 \cdot RT \cdot \log\ {}^{i}p^{*}_{T} + [T \cdot\ {}^{i}\Delta S^{*} + RT \times Const] \tag{S11}$$

Using Eq. (S2) to express volatility in terms of saturation concentration ${}^{i}C^{*}_{T}$ (μg m^{-3}) gives:

$${}^{i}\Delta H^{*} = -2.303 \cdot RT \cdot \log\left(\frac{{}^{i}C^{*}_{T} \times RT}{10^{9} \times MW_{i}}\right) + [T \cdot\ {}^{i}\Delta S^{*} + RT \times Const] \tag{S12}$$

Evaluating Eq. (S12) at reference room temperature T=298 K and using R=8.31·10^{-3} kJ mol^{-1} K^{-1}, the expression for thermodynamic coupling between ${}^{i}\Delta H^{*}$ (kJ·mol^{-1}) and ${}^{i}C^{*}_{298K}$ (μg m^{-3}) is derived:

$${}^{i}\Delta H^{*} = -5.7 \times \log\ {}^{i}C^{*}_{298K} + [298 \times\ {}^{i}\Delta S^{*} + 5.7 \times \log MW_{i} + 49.1 + 2.48 \times Const] \tag{S13}$$

when ${}^{i}\Delta S^{*}$ (J mol^{-1} K^{-1}) and MW_i (g mol^{-1}) vary only modestly among OA components and near-ideal behavior is assumed within a mixture, Eq. S13 can be approximated by a linear relationship:

$${}^{i}\Delta H^{*} = -a \times \log\ {}^{i}C^{*}_{298K} + b. \tag{S14}$$

Consistent with this expectation, measured ${}^{i}\Delta H^{*}$ and $\log {}^{i}C^{*}_{298K}$ values generally follow this linear coupling across all mixtures (Figure S1). However, empirical fits to individual mixtures yield slopes (*a*) systematically steeper than the ideal value of −5.7 and intercepts (*b*) that vary substantially.

These deviations reflect apparent volatility behavior in complex OA mixtures, where non-ideal interactions and compositional variability introduce scatter, particularly for mixtures such as

B1–B2 (*Biomass pyrolysis,* Figure S1c), W1a–W1c (*Wood pyrolysis 1,* Figure S1e), W11–W13 (*Wood pyrolysis 2,* Figure S1i), and others. Considering that most species contributing to the observed scatter in the range $0 < \log {}^{i}C^{*}_{298\mathrm{K}} < 6$ along *x*-axis have $MW_i \sim 100 - 250$ g mol^{-1} and typical ${}^{i}\Delta S^{*} \sim 80 - 120$ J mol^{-1} K^{-1};[21] the term $298 \times {}^{i}\Delta S^{*} + 5.7 \times \log MW_i$ of Eq. (S13) contributes ~35 − 50 kJ mol^{-1} to the intercept, consistent with the observed spread in Figure S1. It follows that the intercept *b* is not strictly constant but varies among species within each mixture due to differences in ${}^{i}\Delta S^{*}$. Figure S2 further shows that this variability correlates with molecular descriptors, such as *MW, AI, O/C* and *H/C*, indicating that entropy contributions ${}^{i}\Delta S^{*}$ depend systematically on species' molecular differences.

The observed steeper empirical slopes also arise from volatility-dependent entropy variations. Taking the derivative of Eq. (S13):

$$\frac{d\ {}^{i}\Delta H^{*}}{d\log\ {}^{i}C^{*}_{298K}} \approx -5.7 + 298 \frac{d\ {}^{i}\Delta S^{*}}{d\log\ {}^{i}C^{*}_{298K}} \tag{S15}$$

and using the observed slopes of ~ −11 kJ mol^{-1} decade^{-1} (Figure S1):

$$\frac{d\ {}^{i}\Delta S^{*}}{d\log\ {}^{i}C^{*}_{298K}} \approx \frac{(-11+5.7)\mathrm{kJ\ mol^{-1}}}{298K} \approx -18\ \mathrm{J \cdot mol^{-1} K^{-1} decade^{-1}} \tag{S16}$$

This entropy variation is modest (~15 − 20% of typical vaporization entropies ~80 − 120 J mol^{-1} K^{-1})[21] and corresponds to ~5 kJ mol^{-1} at 298 K, consistent with expected differences in molecular structure, functionalization, and intermolecular interactions across OA constituents in individual mixtures. Additionally, Figure S3 demonstrates that the mixture-specific data are reproducible, as illustrated by triplicate measurements of the B1 mixture. This reproducibility indicates that the observed scatter along with fitted values of slope and intercept reflect primarily variability in ${}^{i}\Delta S^{*}$ among individual components, rather than measurement uncertainty. Therefore, both the slope *a* and intercept *b* in Eq. (S14) reflect the combined effects of composition-dependent entropy changes, non-ideal mixing, matrix effects, and the fact that both ${}^{i}\Delta H^{*}$ and ${}^{i}C^{*}_{298K}$ are apparent, mixture-specific quantities, rather than intrinsic properties of pure compounds.

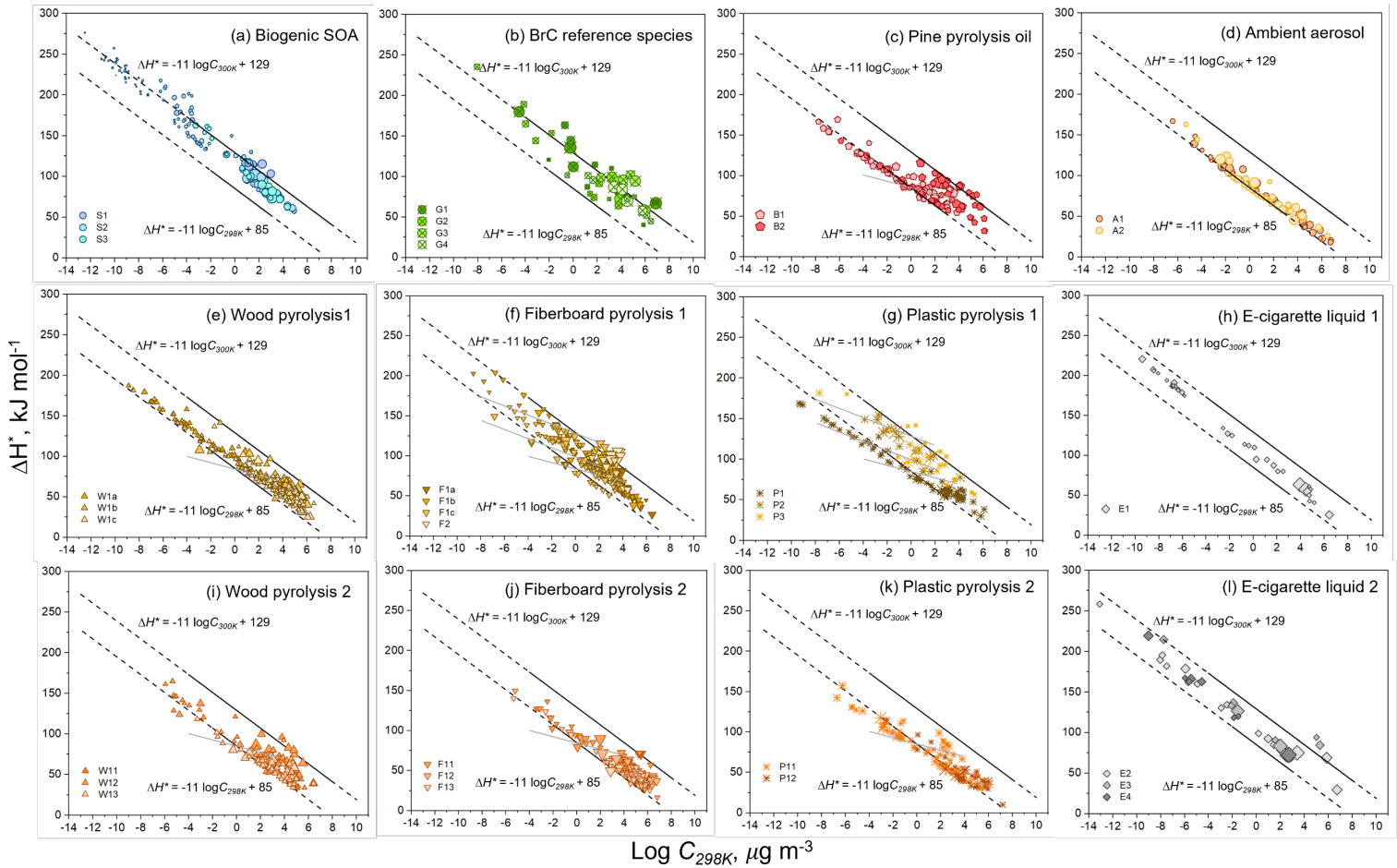

Figure S1. Apparent values of ${}^{i}\Delta H^{*}$ and $\log {}^{i}C^{*}_{298K}$ for individual species measured across various OA mixtures corresponding to the same datasets shown in Figure 1 subdivided here between twelve panels for improved visualization. The upper and lower reference lines correspond to biogenic SOA and anthropogenic OA trends reported by *Epstein et al.*[22] and *Ranjan et al.*[23], respectively. Solid line segments indicate the originally reported ranges, while dashed segments denote extrapolations. Marker size is scaled to the cube root of mass spectral peak intensity. The trend from *May et al.*[24] for biomass-burning OA is shown in panels c, e, f, g, i, j, and k. Additional trends from *Donahue et al.*[25] and *Stolzenburg et al.*[26] for highly oxygenated OA are included in panels f and g. Each data point represents an elemental formula-resolved feature and may include contributions from unresolved structural isomers associated with the same elemental composition

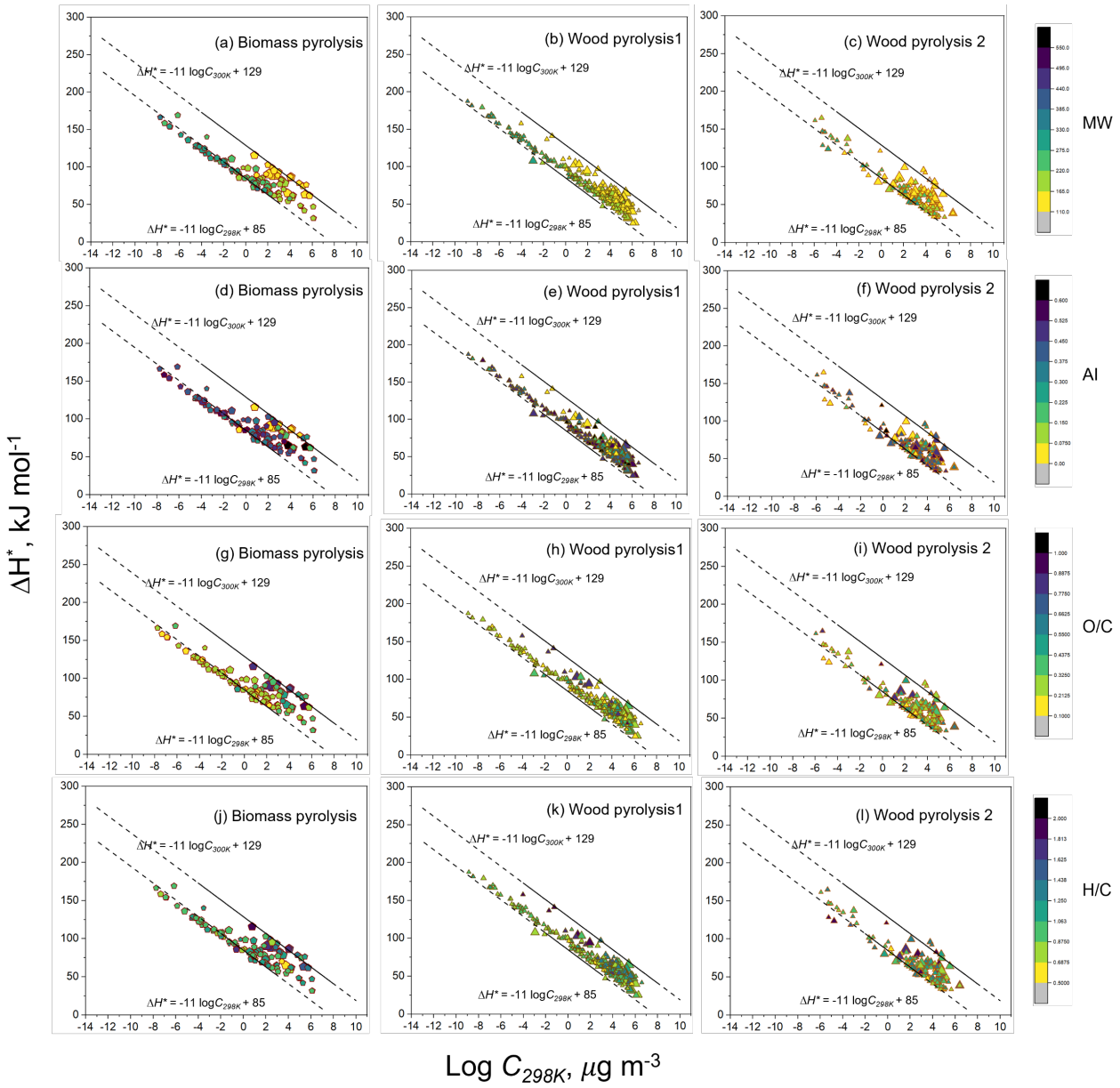

Figure S2. Apparent values of ${}^{i}\Delta H^{*}$ and $\log {}^{i}C^{*}_{298K}$ for individual species from three representative OA mixtures (subset of Figure S1), with data points color-coded by the molecular descriptors of *MW, AI, O/C* and *H/C*. The spread of data within the range $0 < \log {}^{i}C^{*}_{298K} < 6$ correlates with systematic variability in these molecular metrics, indicating differences in the entropy contributions ${}^{i}\Delta S^{*}$. Symbol shapes, sizes, and legends are consistent with Figure S1 to facilitate visual comparison. Each data point represents an elemental formula-resolved feature and may include contributions from unresolved structural isomers associated with the same elemental composition.

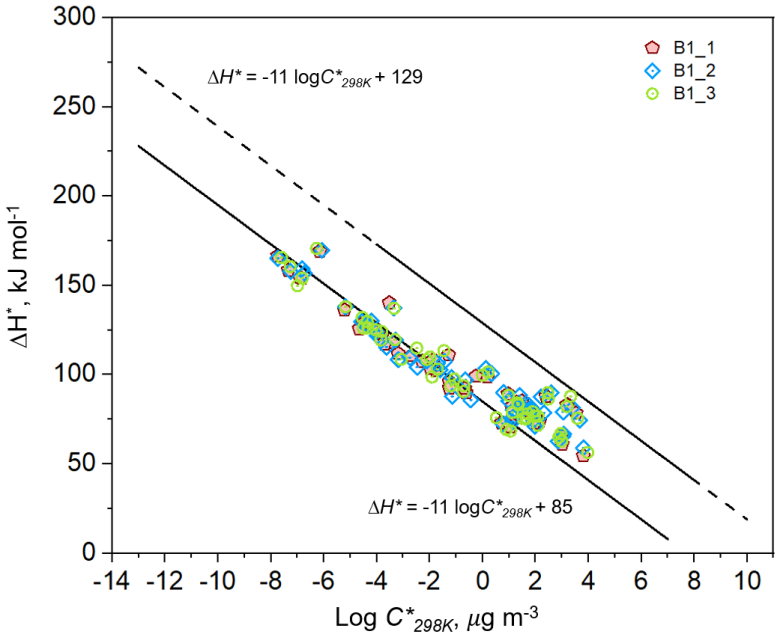

Figure S3. Apparent ${}^{i}\Delta H^{*}$ and $\log {}^{i}C^{*}_{298K}$ values for individual species from triplicate measurements of the B1 mixture (subset of Figure S1, panel c). The scatter patterns are consistent across replicates, with only minor measurement-related variability, indicating that component-specific ${}^{i}\Delta S^{*}$ variability is the primary driver of the observed spread. Each data point represents an elemental formula-resolved feature and may include contributions from unresolved structural isomers associated with the same elemental composition.

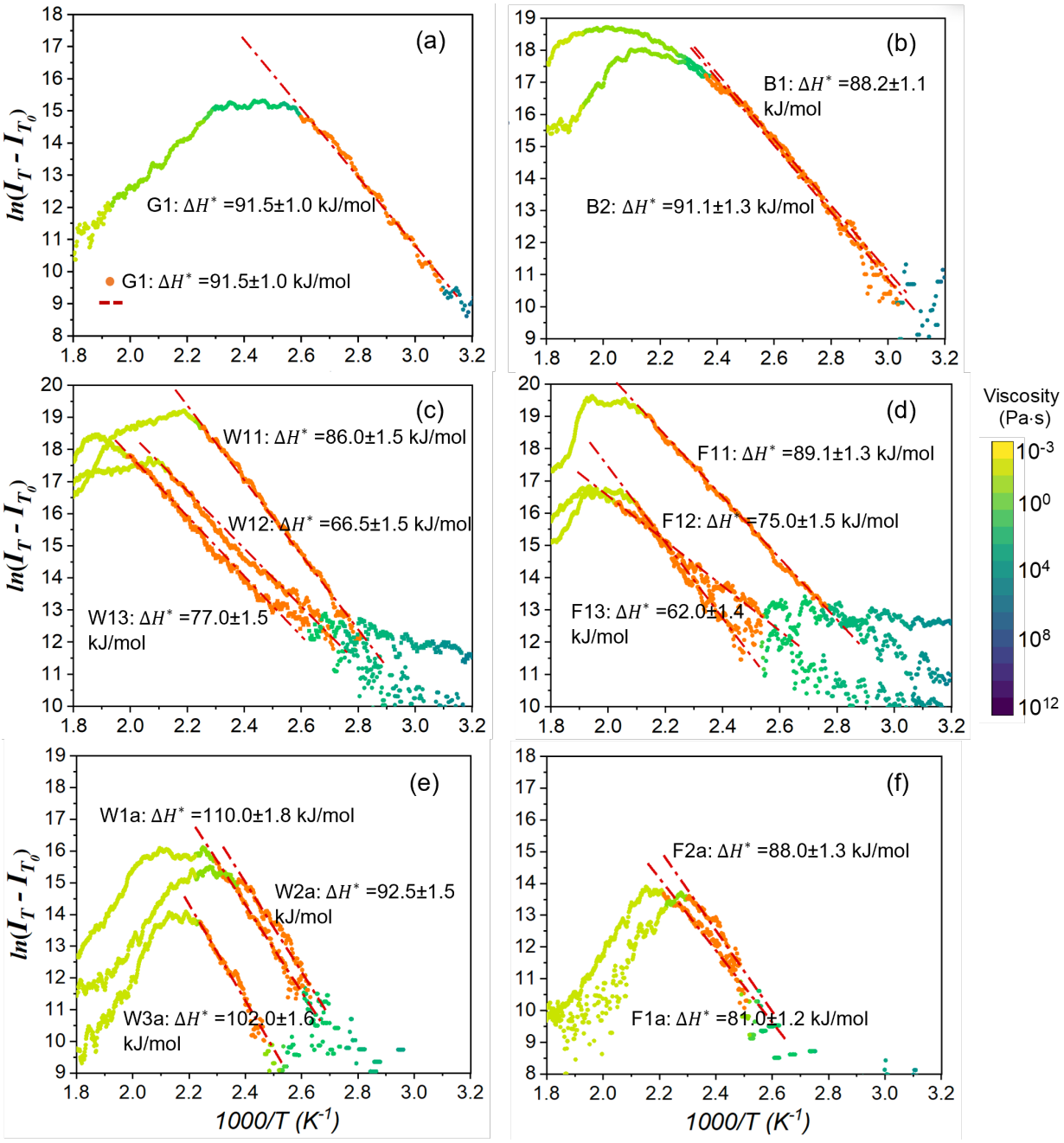

Figure S4. Arrhenius plots of $ln(I_T - I_{T0})$ versus $1/T$ (K^{-1}) of levoglucosan ($C_6H_{10}O_5$) in mixtures of (a) reference, (b) pine pyrolysis oil, (c, e) wood pyrolysis, and (d, f) fiberboard pyrolysis. Orange symbols denote linear regions used to fit (red dashed lines) the data using Clausius−Clapeyron equation and calculate the apparent enthalpies of solid-to-gas transitions, shown in legends. The color scale reflects viscosity values calculated for each species as a function of temperature during the TPD run. Each temperature-resolved record corresponds to an elemental formula-resolved feature which may include contributions from unresolved structural isomers associated with the same elemental composition.

Table S2. Values of ($^{LG}\Delta H^{*}$) and $\log^{LG}C^{*}_{298K}$ measured for pure levoglucosan (p-LG) samples.

Sample No.	**log C^{*}_{298K}** ($\mu g\ m^{-3}$)	**$^{i}\Delta H^{*}$** ($kJ\ mol^{-1}$)	**Ramp rate** ($K\ min^{-1}$)	**Mass concentration[1]** (ppm)	**Sample volume** (ml)	**Mass on the stage[2]** (mg)
1	3.9	85.7	100	100	5	0.50
2	4.1	86.8	50	100	5	0.50
3	3.7	91	70	100	5	0.50
4	4.4	81	70	100	4	0.40
5	4.1	83	70	100	3	0.30
6	4.2	83	70	100	2	0.20
7	4.5	82	70	100	1	0.10
8	3.9	90	70	75	5	0.375
9	4	85	70	75	5	0.375
10	4.1	87	70	75	5	0.375
11	4.1	89	70	1000	5	5.00
12	4	90	70	500	5	2.50
13	4.1	89	70	250	5	1.25
14	4	91	70	100	5	0.50
Average	4.07	86.7	/	/	/	/

1. The LG mass concentration in methanol solvent.
2. The total mass of LG on the tap stage.

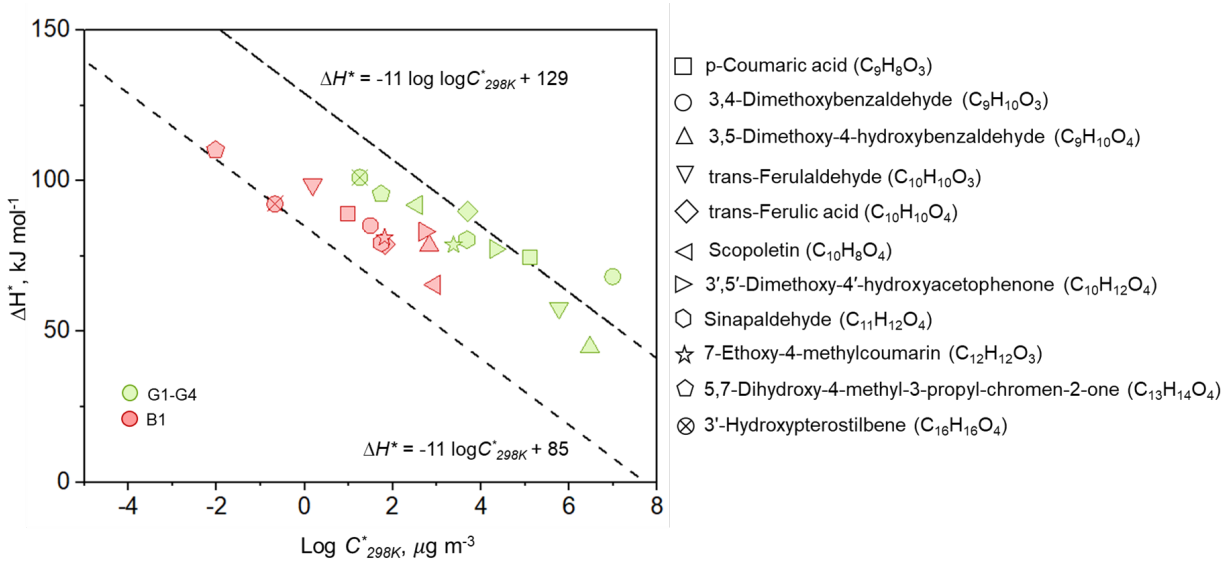

Figure S5. Relationship between apparent enthalpy of condensed-phase to gas-phase transition $^{i}\Delta H^{*}$ and log C^{*}_{298K} of individual species in laboratory-prepared reference blends (G1-G4, green) and pine pyrolysis oil mixtures (B1, red). Symbols denote species with identical elemental formulas (same shape), enabling direct comparison of the related species between G1-G4 and B1 mixtures. Each data point represents an elemental formula-resolved feature and may include contributions from unresolved structural isomers associated with the same elemental composition.

Supplemental Note 3. Details of SHAP model analysis.

To interpret how compound-specific and matrix-dependent properties jointly regulate apparent volatility, we first trained supervised regression models to predict volatility parameters for individual species using the molecular-metric framework defined in Supplemental Note 1. Each observation in the modelling dataset corresponded to one molecular species *i* within a specific OA mixture, paired with its experimentally derived volatility parameters of ${}^{i}\Delta H^{*}$ and $\log({}^{i}p^{*}_{298K})$. The predictor space was restricted to the same 16 features analyzed in the main text. For each molecular metric (*mm = MW, OS$_C$, H/C, O/C, N/C, AI, DBE*, and T_g), we used both the compound-specific, mole-fraction-weighted terms $mm_i \times x_i$ and the corresponding mixture-averaged terms $\langle mm_i \times x_i \rangle = \Sigma_j(mm_j \times x_j)$. This paired design allows the model to account simultaneously for intrinsic molecular characteristics and the bulk mixture environment that defines the apparent volatility.

Model fitting was carried out in R (version 4.3.3) using the H_2O machine-learning platform and its AutoML workflow.[27] For each target variable, the full dataset was randomly split into training (80%) and held-out test (20%) subsets using a fixed random seed to ensure reproducibility. AutoML was configured to train up to 20 candidate regression models on the training subset under default settings and to rank them using cross-validated performance. The best-performing gradient boosted machine (GBM) model was retained and used for the subsequent feature-attribution analysis, and SHAP values reported below were computed using the held-out test subsets.[28] Model performance metrics are summarized in Table S3, including Sample number (n), Fractional Bias (FB), Fraction of predictions within a factor of two (FAC2), Root Mean Squared Error (RMSE), IOA index of agreement and IOAr refined index of agreement.

We used mean absolute SHapley Additive exPlanations (SHAP) approach to evaluate the relative importance of each $mm_i \times x_i$, and $\langle mm_i \times x_i \rangle$ feature in influencing the model predictions. SHAP values, derived from cooperative game theory,[29] quantify the contribution of each feature to the difference between the model prediction using the full feature set and the mean prediction obtained across all possible feature subsets.[30] For the selected model $f_*(.)$ and the i^{th} individual specie represented by a feature vector $y^i = (y^i_{mm})$, the SHAP value for a specific feature p is computed as follows:

$$\phi_p(f_*, y^i) = \sum_{S \subseteq N \setminus \{p\}} \frac{|S|!(|N|-|S|-1)!}{|N|!} \left(f_*\left(x_S^i \cup \{y_p^i\}\right) - f_*\left(y_S^i\right) \right) \quad (17)$$

Here, y_S denotes the instance y with only the features in subset S present; N is the set of all input features; $S \subseteq N \setminus \{p\}$ represents any subset features excluding feature p; $f_*\left(y_S^i\right)$ is the model prediction using only the features in subset S; and $f_*\left(x_S^i \cup \{y_p^i\}\right)$ is the model prediction when the feature subset S is augmented with p. By averaging the absolute SHAP values for feature p, we obtained a measure of its global importance, termed I_p or mean |SHAP|, as:

$$I_p = \frac{1}{m} \sum_{i=1}^{m} \left| \phi_p(f_*, y^i) \right| \quad (18)$$

where m is the total number of instances in the dataset. The concept of the 'mean |SHAP|' value emphasizes the magnitude of feature attribution, providing a more informative and detailed measure of feature importance than traditional approaches based on performance degradation following random feature shuffling. SHAP summary plots were used to illustrate both the magnitude and direction of feature effects across all predictions. To further examine the marginal relationships between individual features and the target variables ${}^{i}\Delta H^{*}$ and $\log({}^{i}p^{*}_{298K})$, we employed partial dependence plots, which visualize the predicted response over a range of feature values while averaging out the influence of all other features.

Table S3. Model performance metrics.

	n	FB	FAC2	r	RMSE	IOA	IOAr
${}^{i}\Delta H^{*}$	1548	0.002	0.987	0.903	18.857	0.689	0.831
$\log({}^{i}p^{*}_{298K})$	1548	0.014	0.890	0.914	1.704	0.801	0.912
$\log({}^{i}C^{*}_{298K})$	1548	0.014	0.791	0.912	1.684	0.712	0.843

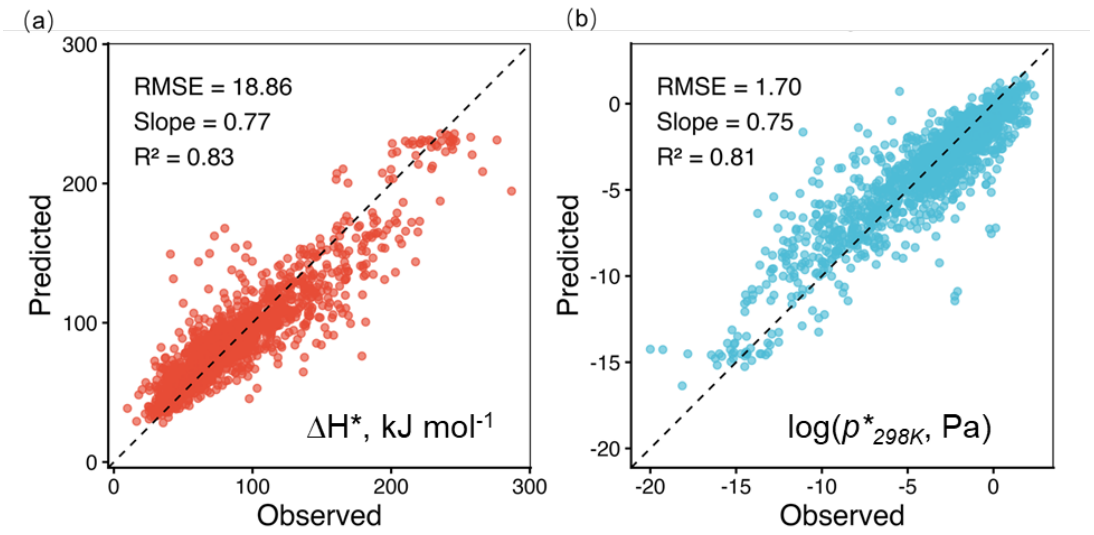

Figure S6. Performance summary of the GMB model for the two volatility targets: (a) ${}^{i}\Delta H^{*}$ and (b) $\log({}^{i}p^{*}_{298K})$. Plots show predicted versus observed values aggregated across all test points, with mean RMSE, R^2, and regression slope indicated. The dashed line represents the 1:1 relationship.

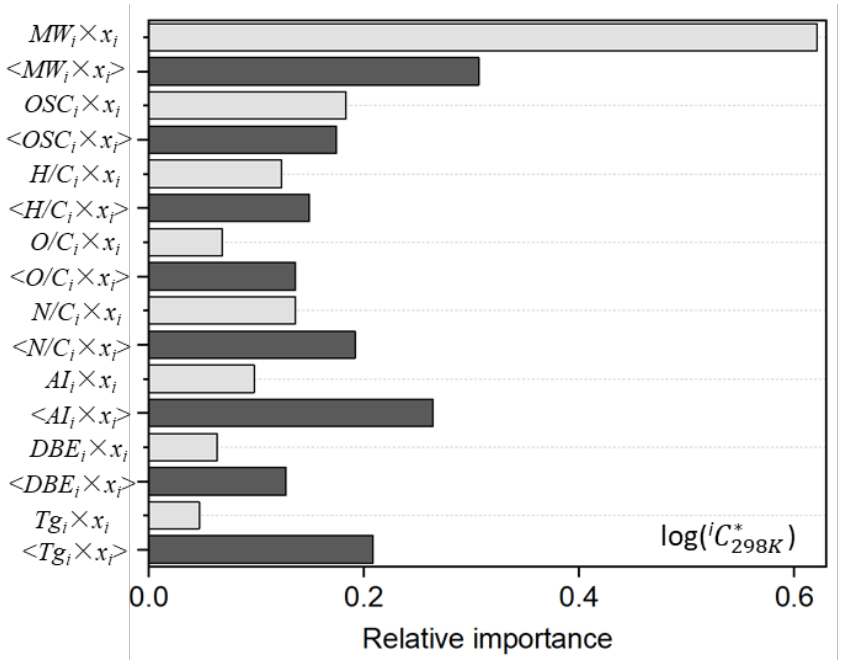

Figure S7. Relative importance of compound-specific (light-colored bars) and mixture-averaged (dark-colored bars) molecular metrics to variations in $\log({}^{i}C^{*}_{298K})$ for individual species, as quantified by SHAP analysis. Except for the compound-specific $MW{\times}x_i$ metric, mixture-averaged metrics consistently exert greater influence than their compound-specific counterparts, underscoring the importance of explicitly accounting for matrix composition when predicting apparent volatility. The elevated importance of $MW{\times}x_i$ reflects its numeric role in the definition of ${}^{i}C^{*}_{298K}$ rather than a dominant physical control.

Supplemental Note 4. Details of WRF-Chem atmospheric simulations.

WRF-Chem version 4.2 is used to simulate trace gases and aerosols during a biomass burning event in the southeastern US in March 2025. The simulations are conducted at 12 km horizontal resolution over a domain of 1836 km by 2160 km. The Whole Atmosphere Community Climate Model (WACCM)[31] global model provided chemical initial and boundary conditions for trace gases and aerosols. The high-resolution rapid refresh (HRRR) model analyses[32] were used to provide the meteorological initial and boundary conditions. The meteorological and chemical conditions were spun up 24 h prior to the simulation period of March 16-19, 2025. The chemical conditions of the spin-up run were used as initial conditions to the simulation period, thus creating continuous chemistry over the entire simulation period. The two BB influenced days discussed in the results are March 18 and 19, 2025.

The gas-phase and aerosol-phase chemistry used in these simulations is described in detail in Shrivastava et al. (2024)[33] with the most relevant aspects to the study described here. Gas-phase chemistry follows the Statewide Air Pollution Research Center (SAPRC-99) mechanism. The Model for Simulating Aerosol Interactions and Chemistry (MOSAIC)[34] represents inorganic aerosol chemistry, the aerosol size distribution, and aerosol microphysics. Particle-phase species are represented in 20 particle size sections from 1 nm to 10 μm.

Emissions from sources other than biogenic and biomass burning (BB) sources are derived from the United States Environmental Protection Agency's 2017 National Emissions Inventory (NEI2017). Volatile chemical product (VCPs) emissions are included using the VCPy framework[35]. Meteorological-dependent biogenic emissions are calculated online from the Model of Emissions of Gases and Aerosols from Nature (MEGAN v2.1)[36] coupled with the community land model version 4 (CLM4) WRF-Chem. Primary BB emissions for both gases and aerosols are from the Quick Fire Emissions Database (QFED). For computational efficiency, primary BB OA is represented by a single semi-volatile species with a C^* of 1 μg m^{-3}. The BB POA is allowed to partition to the gas-phase and subsequently react with OH to contribute to BB SOA.

Simulation of BB SOA formation follows the approach of Shrivastava et al. (2024).[33] For the base case simulation, BB SOA uses a 4-product VBS with C^* of 0.01, 1, 10, and 100 μg m^{-3}. BB SOA is formed from two volatile precursor classes: oxygenated aromatics (such as phenols) and

the other category which represents all remaining SOA precursors associated with BB including heterocyclics, aromatic hydrocarbons, and biogenic VOCs, including acyclic VOCs[37, 38]. The two volatile precursor classes react with OH with reaction rates k_{OH} producing oxidized species corresponding to the volatility bins (with C^* of 0.01, 1, 100 and 10^4 μg m^{-3}**)** with the mass yields and reaction rates shown in Table S3. These species further undergo multigeneration aging with OH radicals with rates of k_{OH}, aging, moving them to successively lower volatility bins. To assess the implications of lower volatility, three sensitivity simulations are conducted which shift the original BB SOA volatilities 1, 2, and 3 orders of magnitude lower. Thus, for example, a 1 order of magnitude shift implies the new volatilities of species in Table S4 will be 0.001, 0.1, 10 and 1000 μg m^{-3}, respectively, with everything else as documented above. All other aspects of the WRF-Chem simulations are consistent between the base case and the sensitivity simulations.

Table S4. VBS_{SOM} parameters used in the WRF-Chem simulations to represent SOA formation from two different biomass burning precursor classes.

VOC Surrogate	k_{OH} **(cm^3 $molec^{-1}$ s^{-1})**	**MW (g mol^{-1})**	**Volatility bin C^* (μg m^{-3})**				$k_{OH,aging}$
			0.01	**1**	**100**	**10000**	
Oxygenated aromatics	6.3×10^{-11}	117	0.3046	0.2215	0.000	0.4740	2.053×10^{-12}
Other precursors	7.2×10^{-11}	102	0.0194	0.1042	0.2450	0.6314	7.345×10^{-13}

Average emissions ratios of other precursors and oxygenated aromatics classes with respect to CO were estimated as 25.9 and 9.5 ppb/ppm-CO, respectively based on chamber experiments performed and reported in Akherati et al. (2020).[38] The yields and rates for these two classes were originally implemented into WRF-Chem in Shrivastava et al. (2024).[37]

CCN number concentrations at 0.5% supersaturation were diagnosed using κ-Köhler theory from WRF-Chem predicted number particle side distributions (PSD), where volume-weighted hygroscopicity (κ) was computed for each PSD size bin assuming internal mixing among all chemical components. The PSD spans 20 bins from 1 nm to 10 μm, with distinct κ values assigned to primary and secondary organic aerosols and inorganic aerosols. Particles with critical supersaturations at or below 0.5% were integrated across the size distribution to yield CCN

concentrations, providing a physically consistent estimate of cloud droplet-forming potential linked directly to the simulated aerosol composition and size; BB SOA and POA were assigned κ values of 0.17 and 0.07, respectively.[39]

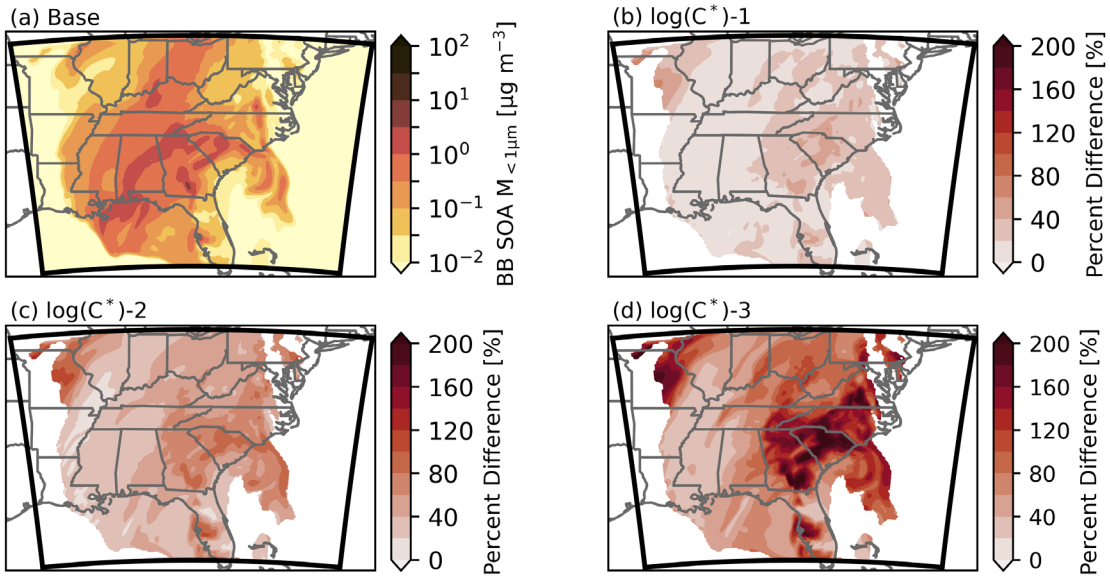

Figure S8. WRF-Chem–simulated mass loadings of submicron biomass-burning (BB) SOA across the southeastern USA modeling domain on March 19, 2025 at 20 UTC, using the QFED fire emissions dataset[33]. (a) Base-case simulation employing the default VBS distribution. (b–d) Percent differences in BB SOA mass loadings relative to the base case for simulations in which the VBS log (C^*) bins are shifted lower by one-, two-, and three-unit values, respectively.

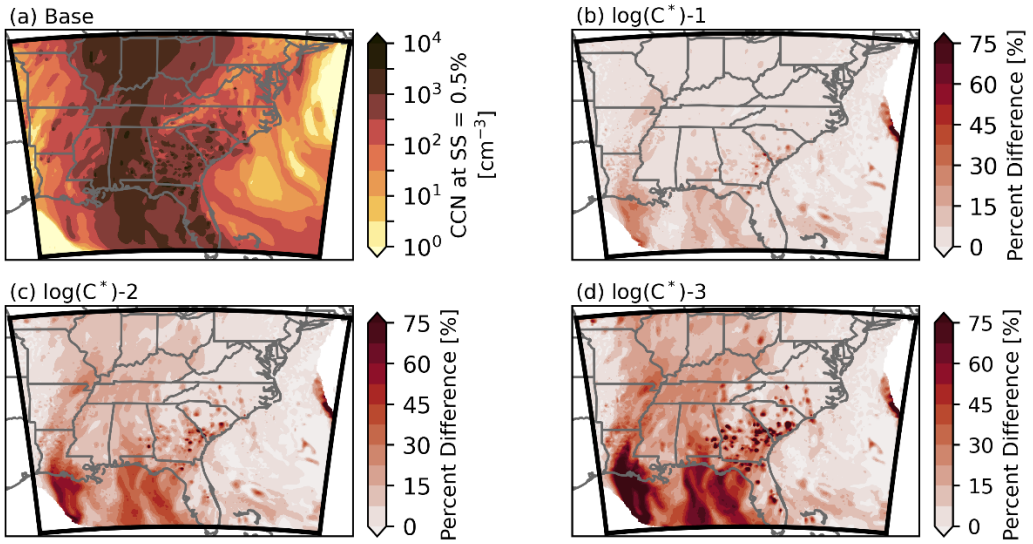

Figure S9. WRF-Chem simulated CCN number concentrations across the southeastern USA, derived from the OA mass loadings shown in Figure 4 at a supersaturation of *S*=0.5%. (a) Base-case simulation. (b–d) Percent differences in CCN concentrations relative to the base case for simulations with progressively reduced VBS log(*C**) bins.

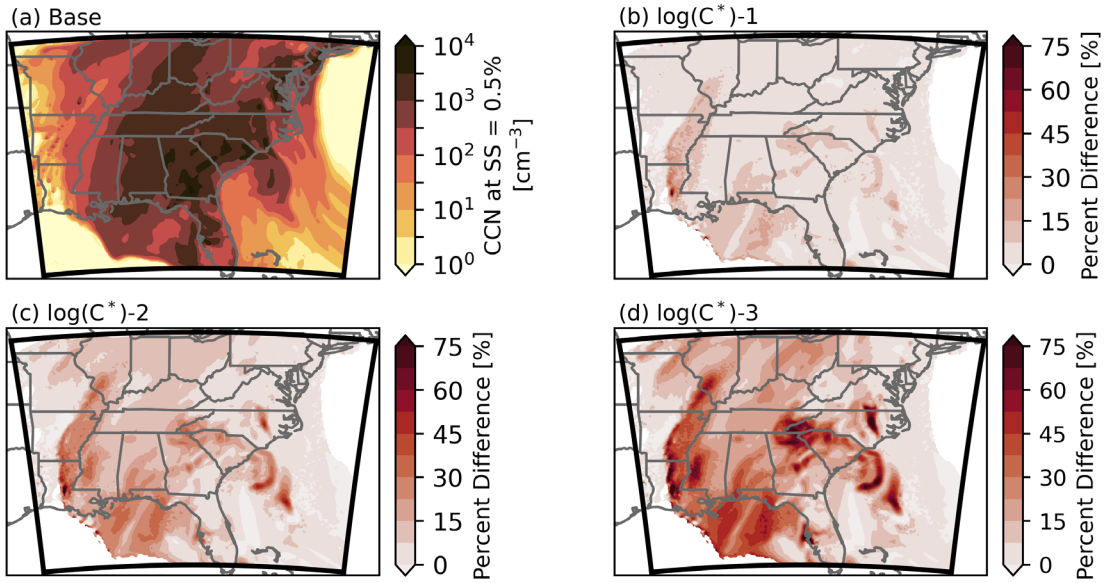

Figure S10. WRF-Chem simulated CCN number concentrations across the southeastern USA, derived from the OA mass loadings shown in Figure S8 at a supersaturation of SS=0.5%. (a) Base-case simulation. (b–d) Percent differences in CCN concentrations relative to the base case for simulations with progressively reduced VBS log(C^*) bins.

References

(1) West, C. P.; Hsu, Y.-J.; MacFeely, K. T.; Huston, S. M.; Aridjis-Olivos, B. P.; Morales, A. C.; Laskin, A. Volatility Measurements of Individual Components in Organic Aerosol Mixtures Using Temperature-Programmed Desorption–Direct Analysis in Real Time–High Resolution Mass Spectrometry. *Anal. Chem.* **2023**, *95* (19), 7403-7408. DOI: 10.1021/acs.analchem.3c00923.

(2) Xie, Q.; Gerrebos, N. G. A.; Calderon-Arrieta, D.; Morton, I. S.; Halpern, E. R.; Li, C.; Zeng, M. F.; Bertram, A. K.; Rudich, Y.; Laskin, A. Molecular Insights into Gas–Particle Partitioning and Viscosity of Atmospheric Brown Carbon. *Environ. Sci. Technol.* **2024**, *58* (41), 18284-18294. DOI: 10.1021/acs.est.4c05650.

(3) Xie, Q.; Halpern, E. R.; Zhang, J.; Shrivastava, M.; Zelenyuk, A.; Zaveri, R. A.; Laskin, A. Volatility Basis Set Distributions and Viscosity of Organic Aerosol Mixtures: Insights from Chemical Characterization Using Temperature-Programmed Desorption–Direct Analysis in Real-Time High-Resolution Mass Spectrometry. *Anal. Chem.* **2024**, *96* (23), 9524-9534. DOI: 10.1021/acs.analchem.4c01003.

(4) Jaitly, N.; Mayampurath, A.; Littlefield, K.; Adkins, J. N.; Anderson, G. A.; Smith, R. D. Decon2LS: An open-source software package for automated processing and visualization of high resolution mass spectrometry data. *BMC bioinformatics* **2009**, *10* (1), 87.DOI: http://www.biomedcentral.com/1471-2105/10/87.

(5) Roach, P. J.; Laskin, J.; Laskin, A. Higher-order mass defect analysis for mass spectra of complex organic mixtures. *Anal. Chem.* **2011**, *83* (12), 4924-4929. DOI: 10.1021/ac200654j.

(6) Chattopadhyay, S.; Tobias, H. J.; Ziemann, P. J. A method for measuring vapor pressures of low-volatility organic aerosol compounds using a thermal desorption particle beam mass spectrometer. *Anal. Chem.* **2001**, *73* (16), 3797-3803. DOI: 10.1021/ac010304j.

(7) McLafferty, F. W.; Turecek, F. *Interpretation of Mass Spectra*; University Science Books, 1993. Koch, B. P.; Dittmar, T. From mass to structure: an aromaticity index for high-resolution mass data of natural organic matter. *Rapid Commun. Mass Spectrom.* **2016**, *30* (1), 250-250. DOI: 10.1002/rcm.7433.

(8) DeRieux, W.-S. W.; Li, Y.; Lin, P.; Laskin, J.; Laskin, A.; Bertram, A. K.; Nizkorodov, S. A.; Shiraiwa, M. Predicting the glass transition temperature and viscosity of secondary organic material using molecular composition. *Atmos. Chem. Phys.* **2018**, *18* (9), 6331-6351.DOI: 10.5194/acp-18-6331-2018.

(9) Li, Y.; Day, D. A.; Stark, H.; Jimenez, J. L.; Shiraiwa, M. Predictions of the glass transition temperature and viscosity of organic aerosols from volatility distributions. *Atmos. Chem. Phys.* **2020**, *20* (13), 8103-8122.DOI: 10.5194/acp-20-8103-2020.

(10) Xie, Q.; Nikkho, S.; Golay, Z.; Morton, I.; Halpern, E.; VanGundy, R.; Zelenyuk, A.; Shrivastava, M.; Zaveri, R. A.; Bertram, A. K.; et al. Distinct Gas-Particle Partitioning and Viscosity Characteristics of Secondary Organic Aerosols Derived from α-Pinene Versus Ocimene. *ACS ES&T-Air* **2025**, *2*, 1916−1926.DOI: 10.1021/acsestair.5c00108.

(11) West, C. P.; Mesa Sanchez, D.; Morales, A. C.; Hsu, Y.-J.; Ryan, J.; Darmody, A.; Slipchenko, L. V.; Laskin, J.; Laskin, A. Molecular and Structural Characterization of Isomeric Compounds in Atmospheric Organic Aerosol Using Ion Mobility-Mass Spectrometry. *The Journal of Physical Chemistry A* **2023**, *127* (7), 1656-1674. DOI: 10.1021/acs.jpca.2c06459.

(12) Moschos, V.; Christensen, C.; Mouton, M.; Fiddler, M. N.; Isolabella, T.; Mazzei, F.; Massabò, D.; Turpin, B. J.; Bililign, S.; Surratt, J. D. Quantifying the Light-Absorption Properties and Molecular Composition of Brown Carbon Aerosol from Sub-Saharan African Biomass Combustion. *Environ. Sci. Technol.***2024**, *58* (9), 4268-4280. DOI: 10.1021/acs.est.3c09378.

(13) Hopstock, K. S.; Xie, Q.; Alvarado, M. A.; Moschos, V.; Bililign, S.; Surratt, J. D.; Laskin, A.; Nizkorodov, S. A. Molecular Characterization and Photoreactivity of Organic Aerosols Formed from Pyrolysis of Urban Materials during Fires at the Wildland–Urban Interface. *ACS ES&T Air* **2024**, *1*

(11), 1495-1506. DOI: 10.1021/acsestair.4c00215.

(14) Xie, Q.; Gerrebos, N.; Calderon-Arrieta, D.; Morton, I.; Halpern, E. R.; Li, C.; Zeng, M.; Bertram, A. K.; Rudich, Y.; Laskin, A. Molecular Insights into Gas-Particle Partitioning and Viscosity of Atmospheric Brown Carbon. *Environ. Sci. Technol.* **2024**, *58* (41), 18284–18294 DOI: doi: 10.1021/acs.est.4c05650

(15) Calderon-Arrieta, D.; Morales, A. C.; Hettiyadura, A. P. S.; Estock, T. M.; Li, C.; Rudich, Y.; Laskin, A. Enhanced Light Absorption and Elevated Viscosity of Atmospheric Brown Carbon through Evaporation of Volatile Components. *Environ. Sci. Technol.* **2024**, *58* (17), 7493-7504. DOI: 10.1021/acs.est.3c10184.

(16) Hettiyadura, A. P. S.; Garcia, V.; Li, C. L.; West, C. P.; Tomlin, J.; He, Q. F.; Rudich, Y.; Laskin, A. Chemical Composition and Molecular-Specific Optical Properties of Atmospheric Brown Carbon Associated with Biomass Burning. *Environ. Sci. Technol.* **2021**, *55* (4), 2511-2521. DOI: 10.1021/acs.est.0c05883.

(17) Li, C. L.; He, Q. F.; Schade, J.; Passig, J.; Zimmermann, R.; Meidan, D.; Laskin, A.; Rudich, Y. Dynamic changes in optical and chemical properties of tar ball aerosols by atmospheric photochemical aging. *Atmos. Chem. Phys.* **2019**, *19* (1), 139-163. DOI: 10.5194/acp-19-139-2019.

(18) Xie, Q.; Windwer, E.; Morton, I. S.; Lavin, K. E.; Halpern, E. R.; Nissenbaum, D.; Nizkorodov, S. A.; Rudich, Y.; Laskin, A. Molecular Characterization of Composition and Volatility of Ambient Organic Aerosol Sampled by an UAV-Mounted Portable Aethalometer. *Analytical Chemistry* **2025**, *97*, 17743−17751. DOI: 10.1021/acs.analchem.5c03027.

(19) Hopstock, K. S.; Klodt, A. L.; Xie, Q.; Alvarado, M. A.; Laskin, A.; Nizkorodov, S. A. Photolytic aging of organic aerosol from pyrolyzed urban materials. *Environmental Science: Atmospheres* **2023**, *3* (9), 1272-1285, DOI: 10.1039/D3EA00078H.

(20) Ridgway, K.; Helfrich, A.; Cast, L.; Trujillo, M.; Medina, C.; Davis, A. Y.; Cleary, T. G.; Falkenstein-Smith, R. L.; Bryant, R. A.; Bundy, M. F.; et al. Emissions from Structure Fires: Overview of BHASMA and Results for CO2 and Select Pollutants by Fuel, Combustion Mode, and Scale. *Environ. Sci. Technol.* **2025**, *59* (44), 23926-23937. DOI: 10.1021/acs.est.5c04682.

(21) Kolská, Z.; Růžička, V.; Gani, R. Estimation of the enthalpy of vaporization and the entropy of vaporization for pure organic compounds at 298.15 K and at normal boiling temperature by a group contribution method. *Industrial & engineering chemistry research* **2005**, *44* (22), 8436-8454. DOI: 10.1021/ie050113x.

(22) Epstein, S. A.; Riipinen, I.; Donahue, N. M. A semiempirical correlation between enthalpy of vaporization and saturation concentration for organic aerosol. *Environ. Sci. Technol.* **2010**, *44* (2), 743-748.DOI: 10.1021/es902497z.

(23) Ranjan, M.; Presto, A. A.; May, A. A.; Robinson, A. L. Temperature dependence of gas–particle partitioning of primary organic aerosol emissions from a small diesel engine. *Aerosol Sci. Technol.* **2012**, *46* (1), 13-21.DOI: 10.1080/02786826.2011.602761.

(24) May, A. A.; Levin, E. J. T.; Hennigan, C. J.; Riipinen, I.; Lee, T.; Collett Jr., J. L.; Jimenez, J. L.; Kreidenweis, S. M.; Robinson, A. L. Gas-particle partitioning of primary organic aerosol emissions: 3. Biomass burning. *Journal of Geophysical Research: Atmospheres* **2013**, *118* (19), 11,327-11,338. DOI: 10.1002/jgrd.50828.

(25) Donahue, N. M.; Epstein, S. A.; Pandis, S. N.; Robinson, A. L. A two-dimensional volatility basis set: 1. organic-aerosol mixing thermodynamics. *Atmos. Chem. Phys.* **2011**, *11* (7), 3303-3318. DOI: 10.5194/acp-11-3303-2011.

(26) Stolzenburg, D.; Fischer, L.; Vogel, A. L.; Heinritzi, M.; Schervish, M.; Simon, M.; Wagner, A. C.; Dada, L.; Ahonen, L. R.; Amorim, A.; et al. Rapid growth of organic aerosol nanoparticles over a wide tropospheric temperature range. *Proceedings of the National Academy of Sciences* **2018**, *115* (37), 9122-9127. DOI: doi:10.1073/pnas.1807604115.

(27) LeDell, E.; Poirier, S. H2o automl: Scalable automatic machine learning. In *Proceedings of the AutoML Workshop at ICML*, 2020; Vol. 2020, p 24.

(28) Friedman, J. H. Greedy function approximation: a gradient boosting machine. *Annals of statistics* **2001**, 1189-1232. DOI: https://www.jstor.org/stable/2699986

(29) Shapley, L. S. Stochastic Games*. *Proceedings of the National Academy of Sciences* **1953**, *39* (10), 1095-1100. DOI: doi:10.1073/pnas.39.10.1095.

(30) Lundberg, S. M.; Erion, G.; Chen, H.; DeGrave, A.; Prutkin, J. M.; Nair, B.; Katz, R.; Himmelfarb, J.; Bansal, N.; Lee, S.-I. From local explanations to global understanding with explainable AI for trees. *Nature machine intelligence* **2020**, *2* (1), 56-67.DOI: 10.1038/s42256-019-0138-9.

(31) Gettelman, A.; Mills, M. J.; Kinnison, D. E.; Garcia, R. R.; Smith, A. K.; Marsh, D. R.; Tilmes, S.; Vitt, F.; Bardeen, C. G.; McInerny, J.; et al. The Whole Atmosphere Community Climate Model Version 6 (WACCM6). *J. Geophys. Res.-Atmos.* **2019**, *124* (23), 12380-12403. DOI: 10.1029/2019JD030943.

(32) Dowell, D. C.; Alexander, C. R.; James, E. P.; Weygandt, S. S.; Benjamin, S. G.; Manikin, G. S.; Blake, B. T.; Brown, J. M.; Olson, J. B.; Hu, M. The High-Resolution Rapid Refresh (HRRR): An hourly updating convection-allowing forecast model. Part I: Motivation and system description. *Weather and Forecasting* **2022**, *37* (8), 1371-1395.DOI: 10.1175/WAF-D-21-0151.1.

(33) Shrivastava, M.; Zhang, J.; Zaveri, R. A.; Zhao, B.; Pierce, J. R.; O'Donnell, S. E.; Fast, J. D.; Gaudet, B.; Shilling, J. E.; Zelenyuk, A.; et al. Anthropogenic Extremely Low Volatility Organics (ELVOCs) Govern the Growth of Molecular Clusters Over the Southern Great Plains During the Springtime. *J. Geophys. Res.-Atmos.* **2024**, *129* (21), e2024JD041212. DOI: 10.1029/2024JD041212.

(34) Zaveri, R. A.; Easter, R. C.; Fast, J. D.; Peters, L. K. Model for Simulating Aerosol Interactions and Chemistry (MOSAIC). *J. Geophys. Res.-Atmos.* **2008**, *113* (D13). DOI: 10.1029/2007JD008782.

(35) Seltzer, K. M.; Pennington, E.; Rao, V.; Murphy, B. N.; Strum, M.; Isaacs, K. K.; Pye, H. O. T. Reactive organic carbon emissions from volatile chemical products. *Atmos. Chem. Phys.* **2021**, *21* (6), 5079-5100. DOI: 10.5194/acp-21-5079-2021.

(36) Guenther, A. B.; Jiang, X.; Heald, C. L.; Sakulyanontvittaya, T.; Duhl, T.; Emmons, L. K.; Wang, X. The Model of Emissions of Gases and Aerosols from Nature version 2.1 (MEGAN2.1): an extended and updated framework for modeling biogenic emissions. *Geosci. Model Dev.* **2012**, *5* (6), 1471-1492. DOI: 10.5194/gmd-5-1471-2012.

(37) Shrivastava, M.; Fan, J.; Zhang, Y.; Rasool, Q. Z.; Zhao, B.; Shen, J.; Pierce, J. R.; Jathar, S. H.; Akherati, A.; Zhang, J.; et al. Intense formation of secondary ultrafine particles from Amazonian vegetation fires and their invigoration of deep clouds and precipitation. *One Earth* **2024**, *7* (6), 1029-1043. DOI: 10.1016/j.oneear.2024.05.015

(38) Akherati, A.; He, Y.; Coggon, M. M.; Koss, A. R.; Hodshire, A. L.; Sekimoto, K.; Warneke, C.; de Gouw, J.; Yee, L.; Seinfeld, J. H.; et al. Oxygenated Aromatic Compounds are Important Precursors of Secondary Organic Aerosol in Biomass-Burning Emissions. *Environ. Sci. Technol.* **2020**, *54* (14), 8568-8579. DOI: 10.1021/acs.est.0c01345.

(39) Bougiatioti, A.; Bezantakos, S.; Stavroulas, I.; Kalivitis, N.; Kokkalis, P.; Biskos, G.; Mihalopoulos, N.; Papayannis, A.; Nenes, A. Biomass-burning impact on CCN number, hygroscopicity and cloud formation during summertime in the eastern Mediterranean. *Atmos. Chem. Phys.* **2016**, *16* (11), 7389-7409. DOI: 10.5194/acp-16-7389-2016.